Delta University Scientific Journal
Journal home page: https://dusj.journals.ekb.eg

Performance Evaluation of Data Detection Methods for Orthogonal Time Frequency Space Modulation

Walid Aly Raslan[1], Heba Mohamed Abdel-Atty[2]

[1]*Assistant Professor, Electronics and Communication Engineering Department, Faculty of Engineering, Delta University for Science and Technology, Gamasa, Egypt.*
[2]*Associate professor at Electrical Engineering Department, Faculty of Engineering, Port Said University, Port Said 42524, Egypt*

Correspondence: [Walid A. Raslan.]; [Faculty of Engineering, Delta University for Science and Technology, Gamasa, Egypt.]; Tel [+201225841034]; Email : walid.raslan@ymail.com

ABSTRACT
Sixth generation (6G) wireless networks are envisioned to provide global coverage for the intelligent digital society of the near future, ranging from traditional terrestrial to non-terrestrial networks, where reliable communications in high-mobility scenarios at high carrier frequencies would play a vital role. In such scenarios, the conventional orthogonal frequency division multiplexing (OFDM) modulation, which has been widely used in both the fourth generation (4G) and the emerging fifth generation (5G) cellular systems, is vulnerable to severe Doppler spread. A new two-dimensional modulation technique called Orthogonal Time Frequency Space (OTFS) modulation designed in the delay-Doppler domain is introduced. Through this design, which exploits full diversity over time and frequency, OTFS coupled with equalization converts the fading, time-varying wireless channel experienced by modulated signals such as OFDM into a time-independent channel with a complex channel gain that is roughly constant for all symbols. In this paper, we evaluate and analyze the performance of the OTFS receiver using four data detection algorithms: Single-tap frequency domain equalizer, Linear minimum mean-square error detection (LMMSE), Message passing detection (MP), and Maximum-ratio combining detection (MRC). Further, we extend our study to the variants of OTFS, where the waveform is transmitted with a cyclic prefix (CP) or zero padding (ZP) added to each OTFS frame or block. The simulation results show that the MRC detector can be improved the detection of the OTFS receiver.

Keywords: Orthogonal Time Frequency Space, Delay–Doppler, zero padding, cyclic prefix, Message Passing, Maximal Ratio Combining,

1. Introduction

With the advent of high-speed trains, unmanned aerial vehicles (UAVs), and self-driving cars, there is an urgent need for reliable communications in high-mobility wireless channels. In OFDM, information symbols are transmitted over a single time-frequency resource, which is susceptible to frequency and time-selective fading effects that degrade the error performance in high-mobility wireless channels. On the other hand, Orthogonal Time Frequency Space (OTFS) multiplexes each information symbol over a two-dimensional (2D) orthogonal basis function that spans the entire time and frequency resources. As a result, all information symbols experience a fixed (time-invariant) flat fading equivalent channel [1]. OTFS shows significant advantages over OFDM in delay–Doppler channels. The delay–Doppler domain provides an alternative representation of a time-varying channel geometry modeling mobile terminals and reflectors. Leveraging this representation, the OTFS modulator spreads each information symbol over a two-dimensional (2D) orthogonal basis function, which spans across the entire time-frequency domain required to transmit a frame [2]. Discrete time-frequency samples can be converted to the delay-Doppler domain via a 2D Symplicit Fourier transform. Specifically, the delay Doppler domain is obtained from the time-frequency domain by an inverse Fourier transform along the frequency axis and a Fourier transform along the time axis as in Figure1 [3].

OTFS receivers are studied in the literature. The Message Passing (MP) algorithm data detection for OTFS is introduced in [4], and [5] with low complexity. In [6], the ZP-OTFS Rake receiver has been proposed. The performance of the OTFS receiver with two stages equalized using a rectangular window is evaluated in [7]. Analysis of the performance of detection based on MRC of uncorrelated as well as correlated diversity branches can be found in [8]. The LMMSE detection and other equalization methods were studied in [9]–[13]. In this paper, we analyze and evaluate the performance of the OTFS detection techniques as Single-tap frequency domain equalizer, Linear minimum mean-square error detection (LMMSE), Message passing detection (MP), and Maximum-ratio combining detection (MRC) under the standard channel model EPA and EVA. Additionally, we perform the simulation for different OTFS frame structures with a cyclic prefix (CP) or zero padding (ZP) added to each OTFS frame or block.

The rest of the paper is organized as follows. In Section II, we discuss the OTFS system model. In Section III, the different OTFS frame structures have been summarized. The data detection methods will be described in section IV. The simulation results are provided in Section V. Section VI contains our concluding remarks.

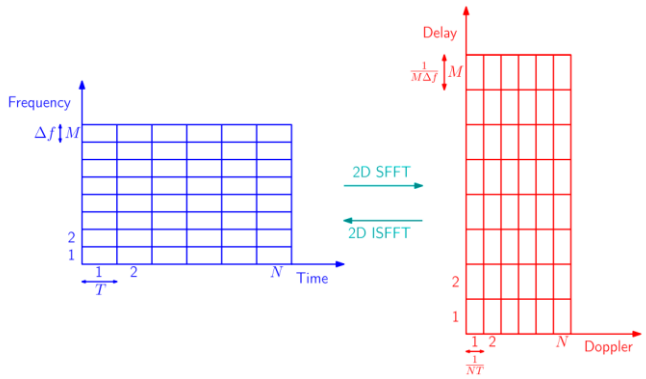

Figure 1: The discrete time-frequency domain and delay-Doppler domain [3].

2. OTFS System Model

The modulation and demodulation of the OTFS system can be shown in Figure 2.

2.1. OTFS modulation

As shown in Figure 2, at the transmitter, $\boldsymbol{X}[m,n]$ represents the delay-Doppler information matrix which contains NM symbols mapping from modulation symbols. Where M and N denote the number of subcarriers and time slots, respectively. The discrete-time domain OTFS frame contains NM samples. Hence, the OTFS frame duration is $T_{\mathrm{f}} = NMT_{\mathrm{s}} = NT$ with the sampling frequency $f_{\mathrm{s}} = B = \frac{1}{\mathrm{T_s}}$ *[14].*

The modulator transforms the symbols from the delay-Doppler domain to the time-frequency domain $\boldsymbol{X_{tf}}[l,k]$ through inverse symplectic fast Fourier transform (ISFFT) as follows:

$$\mathrm{X}_{tf}[l,k] = \frac{1}{\sqrt{NM}} \sum_{n=0}^{N-1} \sum_{m=0}^{M-1} \mathrm{X}[m,n] e^{i2\pi\left(\frac{nk}{N} - \frac{ml}{M}\right)} \qquad (1)$$

where $l = 0,\ldots,M-1, k = 0,\ldots,N-1$.The 2D transformation ISFFT performs two transform operations: i) M-point DFT of the columns of $\boldsymbol{X}$; ii) N-point inverse DFT (IDFT) of the rows of $\boldsymbol{X}$. Then, The transmitted signal $s(t)$ is produced using Heisenberg transform using pulse shaping waveform $g_{tx}(t)$.

$$s(t) = \sum_{n=0}^{N-1} \sum_{m=0}^{M-1} \mathrm{X}_{tf}[l,k] g_{tx}(t-kT) e^{i2\pi\Delta f\,(t-kT)} \qquad (2)$$

2.2. High-mobility channel

Assume high mobility channel response with the number of the channel paths P and B bandwidth, where τ, ν are the channel delay and Doppler shift and can be described as following [6]:

$$\tau_i = \frac{\ell_i}{M\Delta f} \le \tau_{\max} = \frac{\ell_{\max}}{M\Delta f}, \quad \nu_i = \frac{\kappa_i}{NT} \quad |\nu_i| \le \nu_{\max} \qquad (3)$$

where ℓ_i, κ_i represent the normalized delay and Doppler shift, respectively. The continuous time received signal $r(t)$ is given as

$$r(t) = \int g(\tau,\nu)s(t-\tau)d\tau \tag{4}$$

where $g(\tau,t)$ is the delay-time channel response

$$g(\tau,t) = \int_{\nu} h(\tau,\nu)e^{j2\pi\nu(t-\tau)}d\nu \tag{5}$$

where $h(\tau,\nu)$ is the high mobility channel response. The discrete-time form of the received is expressed as

$$r[q] = \sum g^{s}[l,q]s[q-l], \quad q = 0,\ldots,NM-1, \tag{6}$$

where $g^{s}[l,q]$ is the discrete delay-time channel response.

$$g^{s}[l,q] = \sum_{i=1}^{P} g_i z^{\kappa_i(q-l)\delta[l-l_i]} \tag{7}$$

where $z = e^{\frac{j2\pi}{NM}}$, and g_i is the channel gain of the multipath channel. We assume that the delay-Doppler channel is to be fixed over the T_f. To meet this, N may need to be reduced at the expense of lesser Doppler shift resolution [15].

2.3. OTFS demodulation

On the receiver side, the received signal $r(t)$ is transformed to the time-frequency domain by the Wigner transform as follows:

$$\mathbf{Y}_{tf}[l,k] = Y(f,t)\big|_{f=l\Delta f,\,t=kT} = \int r(t')g_{rx}^{*}(t'-t)e^{-j2\pi f(t'-t)}dt' \tag{8}$$

where g_{rx} is the received matched filter. Finally, the delay-Doppler domain samples are obtained by applying symplectic fast Fourier transform (SFFT) on time-domain received samples as

$$\mathbf{Y}[m,n] = \frac{1}{\sqrt{NM}} \sum_{k=0}^{N-1}\sum_{l=0}^{M-1} \mathbf{Y}_{tf}[l,k]e^{-j2\pi(\frac{nk}{N}-\frac{ml}{M})}, \tag{9}$$

The SFFT corresponds to a 2D transformation which takes an *M*-point IDFT of the columns of $\boldsymbol{Y}$ and an *N*-point DFT of the rows of $\boldsymbol{Y}$.

2.4. OTFS input-output relation

For simplicity, we can use the matrix representation for the input-output relation. Then, we can rewrite (6) as

$$\mathbf{r} = \mathbf{G}.\mathbf{s} + \mathbf{w}, \tag{10}$$

where $\boldsymbol{w}$ additive white Gaussian noise (AWGN) with variance σ_w^2, and s is the transmitted samples vector, and $\boldsymbol{G}$ is the channel matrix [16].

The channel matrix $\boldsymbol{G}$ has $l_{max}+1$ nonzero diagonal and subdiagonals, with elements in each subdiagonal given by

$$\mathbf{G}[q,q-l] = g^{s}[l,q] \quad \text{for } l \le q \le NM-1 \tag{11}$$

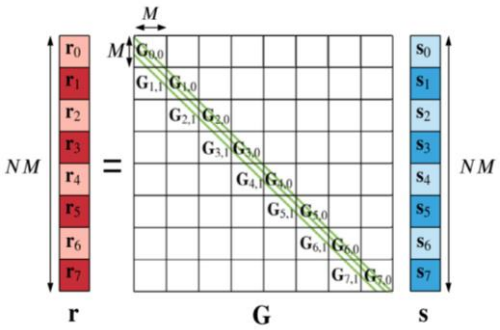

Figure 2: Example of channel matrix $\boldsymbol{G}$ ((l_{max} = 2) and N = 8) [3].

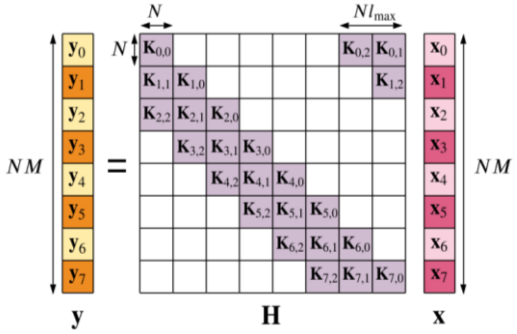

Figure 3: Delay-Doppler channel matrix $\boldsymbol{H}$ with ((l_{max} = 2) and M = 8) [3].

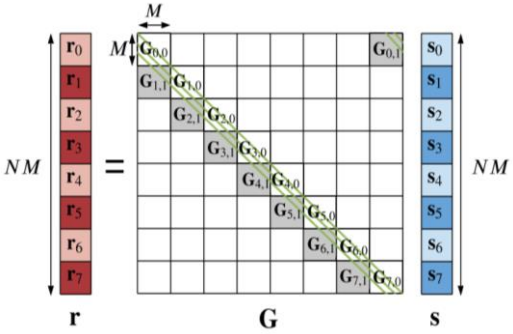

Figure 4: RCP-OTFS time domain channel matrix $\boldsymbol{G}$ with l_{max} = 2 [3].

Figure 3 shows an example describing the channel matrix $\boldsymbol{G}$ with three delay paths (l_{max} = 2) and N = 8. Then the block-wise input-output relation can be written as

$$\begin{aligned} r_0 &= \mathbf{G}_{0,0}.\mathbf{s}_0 + \mathbf{w}_0 && \text{n=0} \\ r_n &= \mathbf{G}_{n,0}.\mathbf{s}_n + \mathbf{G}_{n,0}.\mathbf{s}_{n-1} + \mathbf{w}_0 && 1 \le n \le N\text{-}1 \end{aligned} \tag{12}$$

On the other hand, the delay-Doppler input-output relation can be gotten as

$$\mathbf{y} = \mathbf{H}.\mathbf{x} + \mathbf{z} \tag{13}$$

where $\boldsymbol{H}$ is the delay-Doppler channel matrix and $\boldsymbol{z}$ is the delay-Doppler additive white Gaussian noise (AWGN) [3].

$$\mathbf{H} = (\mathbf{I}_M \otimes \mathbf{F}_N).\tilde{\mathbf{H}}.(\mathbf{I}_M \otimes \mathbf{F}_N^{\dagger}) \tag{14}$$

where $\boldsymbol{F}_M, \boldsymbol{F}_N^{\dagger}$ are the M-point Fourier transform and the N-point Fourier transform.

Let $\boldsymbol{K}_{m,l}$ be the subblocks of channel matrix **H**, representing the delay-Doppler channel block between the m received block and the $[m-l]_M th$ transmitted block. Figure 4 illustrates the delay-Doppler channel matrix with M =8. Recalling the transmitted and received blocks $\boldsymbol{x}_m, \boldsymbol{y}_m$, we obtain the block-wise delay-Doppler input-output relation as

$$\mathbf{y}_m = \sum_{l \in L} \mathbf{K}_{m,l} . \mathbf{x}[m-l]_M + \mathbf{z}_m, \qquad (15)$$

3. Different OTFS frame structures

The OTFS frame structure has different variations as in Figure 5.

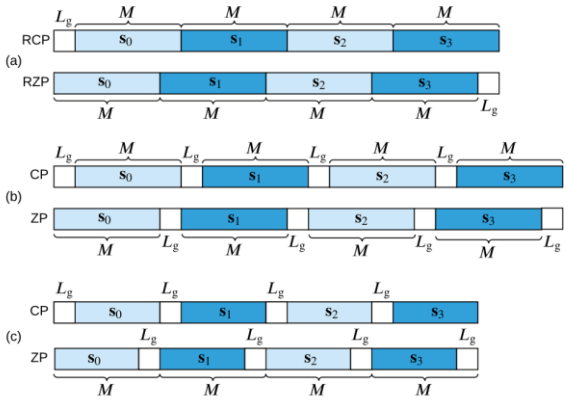

Figure 5: (a) a CP/ZP is added to the frame; (b) a CP/ZP is added to each block; (c) a CP/ZP is included within each block [3].

3.1. Reduced zero padding (RZP) OTFS frame

A single ZP of length l_{max} is appended to the OTFS time frame to intersymbol interference due to the delay spread as shown in Figure 5 (a). (RZP-OTFS has one ZP per frame) [3]. The RZP-OTFS time-domain input-output relation is the same (6). By Omitting noise and substituting $q = m + nM$ into (6) yields [17]

$$\mathbf{r}[m+nM] = \sum_l g^s[l, m+nM]\mathbf{s}[m+nM-l], \qquad (16)$$

We can now narrow it down to each OTFS block. For the nth block, the mth Rx/Tx samples can be rewritten as

$$\mathbf{r}_n[m] = \mathbf{r}[\mathbf{m}+\mathbf{nM}], \qquad (17)$$

and

$$\begin{aligned} \mathbf{s}_n[m-l] &= \mathbf{s}[m+nM-l] \quad for\ m \geq l, \\ \mathbf{s}_n\left[[m-l]_M\right] &= \mathbf{s}[m+nM-l] \quad for\ m < l, \end{aligned} \qquad (18)$$

Then, the element-wise input-output relation can be obtained by substituting (17) and (18) into (16) yields

$$\mathbf{r}_n[m] = \sum_{l, l \leq m} g^s[l, m+nM]\mathbf{s}_n[m-l] + \underbrace{\sum_{l, l \leq m} g^s[l, m+nM]\mathbf{s}_{n-1}\left[[m-l]_M\right]}_{\text{Interblock Interference}} \qquad (19)$$

For the first block ($n = 0$), we set the zero-padding

$$\mathbf{s}_{n-1}\left[[m-l]_M\right] = 0 \quad \text{for } n=0 \text{ and } m<l, \qquad (20)$$

which yields

$$\mathbf{r}_0[m] = \sum_{l, l \le m} g^s[l, m]\mathbf{s}_0[m-l] \tag{21}$$

Implying that the first block $\boldsymbol{s}_0$ is free of interblock interference as no samples are transmitted before the $0-th$ block.

3.2. Reduced cyclic prefix (RCP) OTFS frame

A single CP of length l_{max} is prepended to an OTFS frame as in Figure 5(a), where the CP is the copy of the last l_{max} samples in the frame. At the receiver, the CP is discarded before further processing [18]. As RZP-OTFS frame, the time domain input-output relation is the same as (6). Figure 6 shows the time domain channel matrix for RCP OTFS with $N = 8$. Unlike the case in Figure 3, $\boldsymbol{G}$ is not a lower triangular matrix and has nonzero elements in the top-right corner due to CP. The block-wise input-output relation (12) is reduced to

$$\mathbf{r}_n[m] = \mathbf{G}_{n,0}.\mathbf{s}_n + \mathbf{G}_{n,1}.\mathbf{s}_{[n-1]_N} + \mathbf{w}_n. \tag{22}$$

Alternatively, the block-wise input-output relation (omitting noise for brevity) in (22) can be written in the element-wise format as

$$\mathbf{r}_n[m] = \sum_{l, l \le m} g^s[l, m+nM]\mathbf{s}_n[m-l] + \underbrace{\sum_{l, l \le m} g^s[l, m+nM]\mathbf{s}_{[n-1]_N}\left[[m-l]_M\right]}_{\text{Interblock Interference}} \tag{23}$$

Unlike (19) for RZP-OTFS, the first block s0 will have interference from the CP, which is equivalent to having interference from the last block $\boldsymbol{s}_{N-1}$.

3.3. CP-OTFS frame

As CP-OFDM, the CP-OTFS has CP for each N transmitted block. the time domain input-output relation can be written as

$$\mathbf{r}_{CP}[q] = \sum_{l \in L} g^s[l, q]\mathbf{s}_{CP}[q-l] + \mathbf{w}_{CP}[q], \tag{24}$$

Where $q = 0, \cdots, (M + L_{CP})N - 1$ and $L_{CP} \ge l_{max}$ denotes the length of the CP. After the CP has been removed from the receiver [3]

$$\mathbf{r}_n[m+nM] = \sum_{l \le L} g^s[l, m+n(M+L_{CP})]\mathbf{s}\left[[m-l]_M + nM\right] + \mathbf{w}[m+nM], \tag{25}$$

The block-wise matrix input-output relation can be written as

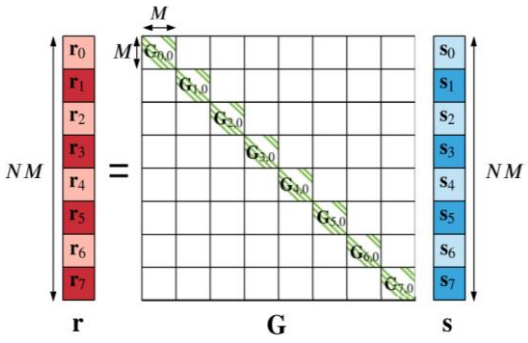

Figure 6: CP-OTFS t time domain channel matrix $\boldsymbol{G}$ with l_{max} = 2 [3].

$$\mathbf{r}_n = \mathbf{G}_{n,0}.\mathbf{s}_n + \mathbf{w}_n \tag{26}$$

The diagonal blocks of channel matrix G can be seen in Fig .6.

$$\mathbf{G}_{n,0}\left[m,[m-l]_M\right] = g^s[l, m+n(M+L_{CP})] \qquad (27)$$

Unlike the RZP/RCP-OTFS in (19) and (23), there is no interblock interference for CP-OTFS thanks to the CP per block

3.4. ZP-OTFS frame

As CP-OTFS, the ZP of length $L_{ZP} \geq lmax$ is added to each of the N time domain blocks. The block-wise input-output of ZP-OTFS is the same (26) and the channel matrix is the same (27) [6].

4. Detection methods

In this section, we illustrate different data detection techniques that can be used for OTFS. We assume a single antenna transmitter and receiver. Additionally, we focus only on data detection methods without channel coding. The four detection methods that have been considered in this paper are:

- Single-tap frequency domain equalizer (1tap)
- Linear minimum mean-square error detection (LMMSE)
- Message passing detection (MP)
- Maximum-ratio combining detection (MRC)

We assume that the OTFS frame has a duration of NT within $M\Delta f$. In the delay-Doppler domain. The samples vectors $\boldsymbol{x}, \boldsymbol{y}$ which contain M blocks of N samples can be obtained by vectorizing the $\boldsymbol{X}^T$ and $\boldsymbol{Y}^T$ [14].

$$\begin{aligned} x &= \begin{bmatrix} x_0 & \cdots & x_{M-1} \end{bmatrix}^T = vec(\mathbf{X}^T) \\ y &= \begin{bmatrix} y_0 & \cdots & y_{M-1} \end{bmatrix}^T = vec(\mathbf{Y}^T) \end{aligned} \qquad (28)$$

Previously we explain the input-output delay-Doppler relation in (13) and delay-Doppler channel matrix $\boldsymbol{H}$ in Figure 4. Then, each received samples vector was given in (15). the matrix H has S nonzero elements in each row, which corresponds to the number of discrete delay-Doppler paths in the delay-Doppler grid. The multipath channel with P paths may result in $S \geq P$, since fractional delay and/or Doppler cause leakage into neighboring grid points for every one of the P paths, when the receiver is sampling, Equality holds ($S = P$) when delay and Doppler shifts of the multipath are exactly integer multiples of delay resolution $1/M\Delta f$ and Doppler resolution $1/NT$ of an OTFS frame, which is not always a practical assumption. Due to the under-spread nature of typical wireless channels, we can assume that $S \ll NM$, which implies that $\boldsymbol{H}$ is a sparse matrix. The sparsity of matrix $\boldsymbol{H}$ combined with other special properties can be used to design efficient detectors for OTFS, which will be discussed in detail in the rest of the section.

4.1. Single-tap frequency domain equalizer

We consider CP-OTFS. We assume static (or very low mobility) multipath channels and rectangular pulse shaping waveforms in the rest of the section, we recall the vectorized time-domain input-output relation in (10), and the corresponding time-frequency domain block-wise input-output relation is [3]

$$\hat{\mathbf{y}}_n = \hat{\mathbf{H}}_{n,0}.\hat{\mathbf{x}}_n + \hat{\mathbf{w}}_n \qquad (29)$$

With

$$\begin{aligned} \hat{\mathbf{H}}_{n,0} &= \mathbf{F}_M.\mathbf{G}_{n,0}.\mathbf{F}_N^{\dagger} \\ \hat{\mathbf{y}}_n &= \mathbf{F}_M.\mathbf{r}_n \end{aligned} \qquad (30)$$

The single tap MMSE equalizer is as in

$$\hat{\mathbf{x}}_n[m] = \frac{\hat{\mathbf{H}}^*_{n,0}[m,m]\hat{\mathbf{y}}_n[m]}{\left|\hat{\mathbf{H}}_{n,0}[m,m]\right|^2 + \sigma_w^2} \qquad (31)$$

where

$$\hat{\mathbf{y}}_n[m] = \hat{\mathbf{H}}_{n,0}[m,m]\hat{\mathbf{x}}_n[m] + \underbrace{\sum_{m'=0,m'\neq m'}^{M-1} \hat{\mathbf{H}}_{n,0}[m,m']\hat{\mathbf{x}}_n[m']}_{\text{Interblock Interference}} + \hat{\mathbf{w}}_n[m] \qquad (32)$$

Which contains the intercarrier interference (ICI) term. The estimated time-frequency domain samples vector is transformed to the time domain using the M-point IFFT operation as

$$\hat{\mathbf{s}}_n = \mathbf{F}_M^{\dagger}.\hat{\mathbf{x}}_n \qquad (33)$$

The estimated delay-Doppler domain symbols vector is obtained as

$$\hat{\mathbf{x}} = (I_M \otimes F_N).\mathbf{P}^T.\hat{\mathbf{s}} \qquad (34)$$

Equations (33) and (34) constitute the SFFT operation to convert the equalized sampled from the frequency-time domain to the delay-Doppler domain. As shown in (31), if there is no noise, the performance of the single tap equalizer depends on the power ratio between the ICI term and the diagonal element $\hat{\boldsymbol{H}}_{n,0}[m,m]$. When the Doppler spread increases as in high mobility wireless channels, the power of the ICI term (from the off-diagonal elements $\hat{\boldsymbol{H}}_{n,0}[m,m']$ increases, thereby leading to performance degradation.

4.2. Linear minimum mean-square error detection

In this subsection, we will discuss the well-known linear minimum mean-square error (LMMSE) detector for OTFS, which can offer good performance in both static and high mobility channels [19]. Recalling the input-output relation in (13), the LMMSE estimate of x is given as

$$\hat{\mathbf{x}} = (\mathbf{H}^{\dagger}.\mathbf{H} + \sigma_w^2 I_{MN})^{-1}.\mathbf{H}^{\dagger}.y \qquad (35)$$

Recalling the time domain input-output relation of RCP/RZP-OTFS in (10), the LMMSE estimate of s is given as

$$\hat{\mathbf{s}} = (\mathbf{G}^{\dagger}.\mathbf{G} + \sigma_w^2 \mathbf{I}_{MN})^{-1}.\mathbf{G}^{\dagger}.\mathbf{r} \qquad (36)$$

The estimated time domain samples are then transformed back to the delay-Doppler domain to obtain the estimated information symbols using the relation in (34). The operation in (36) requires inverting an $NM \times NM$ matrix. Finally, the block estimates are converted back to obtain the delay-Doppler information symbols similar to (34) [9].

4.3. Message Passing Algorithm (MPA) Detection

LMMSE detection can provide good performance in doubly selective channels, but it comes at a high cost in terms of complexity. Single tap equalization, on the other hand, requires the least amount of complexity, but its performance degrades with increasing Doppler shifts. Message Passing Algorithm (MPA) detection can outperform LMMSE detection with much lower complexity and can be applied to all OTFS variants. We now propose a message passing (MPA) detection algorithm for OTFS using the delay-Doppler input-output relation in (13)[13]. From (13), the joint maximum a posteriori probability (MAP) detection rule for estimating the transmitted signals is given by

$$\hat{\mathbf{x}} = \arg \max_{\mathbf{x}\in A^{NM\times 1}} \Pr(\mathbf{x}|\mathbf{y},\mathbf{H}) \qquad (37)$$

The symbol-by-symbol MAP detection rule for $c = 0,\ldots,NM-1$

$$\hat{\mathbf{x}}[c] = \arg \max_{\mathbf{x}\in A^{NM\times 1}} \prod_{d\in\zeta_c} P_r\left(y[d]|x[c] = a_j, \mathbf{H}\right) \qquad (38)$$

Where $A = \{a_1,\ldots,a_Q\}$ is the modulation alphabet of size Q. Let the set of S observation nodes $\{y[d], d \in \zeta(c)\}$ is contained in each variable node $x[c]$. Also, let $a_j \in A$ are equally likely and $[d]$ for all $d \in \zeta_c$ are approximately independent due to the sparsity of $\boldsymbol{H}$. We present an MP detector with linear complexity in NM to solve the approximate symbol-by-symbol MAP detection in (38). The variable $x[c]$ is isolated from the other interference terms for each $y[d]$, which are approximated as Gaussian noise with easily computable mean and variance. The mean and variance of the interference terms are used as messages from observation nodes to variable nodes in the MP algorithm [6]. Figure 8 shows the connections and the messages passed between the observation and variable nodes. The MPA algorithm is given in Algorithm 1.

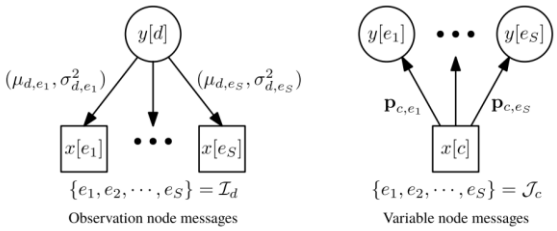

Figure 7: Factor graph to MPA

Algorithm 1: MPA algorithm

Initialization:

pmf $p_{c,d}^{(0)} = \frac{1}{Q}, c = 0, \cdots, NM-1, d \in \zeta(c)$

For $i = 1$ *to* T do $(Number\ of\ iterations)$

Observation nodes $y[d]$ compute the means and variances of Gaussian random variables using $p_{c,d}^{(i-1)}$ and pass them to variables nodes $x[c]$

Variable nodes $x[c]$ update $p_{c,d}^{(i)}$ and pass them to observation nodes $y[d]$

Compute convergence indicator

Update the decision on the transmitted symbols if needed

if (Stopping criteria satisfied) **then EXIT**

End (Decision calculation)

4.4. Maximum-ratio combining detection

The maximum-ratio combining (MRC) detection, offers similar performance to that of the MP detection but at a much lower complexity. The MRC detection method is motivated by the traditional rake receiver in code division multiple access (CDMA) systems since OTFS can be interpreted as a two-dimensional CDMA with information symbols spreading in both time and frequency. In direct sequence CDMA operating in a multipath fading channel, a rake receiver combines the delayed components (or echoes) of the transmitted symbols, which are extracted using matched filters tuned to the respective delay shifts. Similarly, in OTFS, the channel-impaired signal components received at different delay branches can be extracted and coherently combined using diversity combining techniques such as MRC (see Figure 8) to improve the signal-to-noise ratio (SNR) of the accumulated signal [8].

In the MRC detection, we can cancel the estimated interference in the branches selected for combining and iteratively improve the post-MRC signal-to-interference-plus-noise ratio (SINR). In the following, we present the *delay-Doppler* MRC detection. With the effect of the ZP, the delay-Doppler input-output relation (15) can be modified as

$$\mathbf{y}_{m'} = \sum_{l' \in L} \mathbf{K}_{m',l'} \cdot \mathbf{x}_{m'-l'} + \mathbf{z}_{m'}, \qquad (39)$$

Next, we conduct the detection procedure iteratively for estimating $\boldsymbol{x_m}$ only for $m = 0, \ldots, M-1$, since $\boldsymbol{x_m} = \mathbf{0}$ for $m = M, \ldots, M-1$ are the ZP. Algorithm 2 provides the detailed delay-Doppler MRC operation.

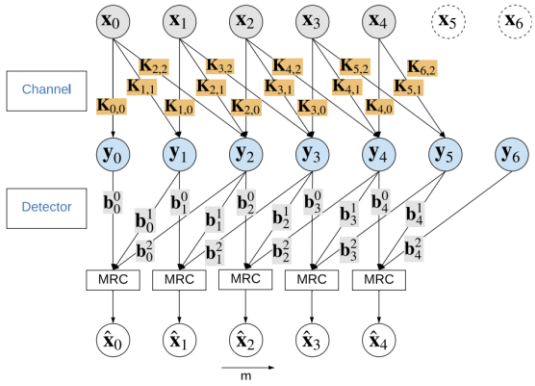

Figure 8: MRC delay-Doppler domain operation

Algorithm 2: MRC algorithm

input:

$x_m = 0$ for $m = 0, \dots, M-1$

channel matrix H and y_m for $m = 0, \dots, M' - 1$

$for\ i = 1\ to\ T$ do $(Number\ of\ iterations)$

$for\ m = 0: M-1$ do

$\boldsymbol{D}_m = \sum_{l \in \mathcal{L}} \boldsymbol{K}_{m+l,l}^{\dagger} \boldsymbol{K}_{m+l,l}$

$for\ l \in \mathcal{L}$ do

$$b_m^l = y_{m+l} - \sum_{l' \neq l} \boldsymbol{K}_{m+l,l'} . \widehat{\boldsymbol{x}}_{m+l-l'}$$

end

$$\boldsymbol{g}_m = \sum_{l \in \mathcal{L}} \boldsymbol{K}_{m+l,l}^{\dagger} \boldsymbol{b}_m^l$$

$$\boldsymbol{c}_m = \boldsymbol{D}_m^{-1} . \boldsymbol{g_m}$$

$$\widehat{\boldsymbol{x}}_m = \boldsymbol{\mathcal{D}}(\boldsymbol{c}_m)$$

Let *D(·)* denote the symbol-by-symbol maximum likelihood detection (MLD)

$$\widehat{\boldsymbol{x}}_m[n] = arg \min_{a_j \in Q} \left| a_j - \boldsymbol{c_m}[\boldsymbol{n}] \right|$$

End

End

Output (Decision calculation)

5. Simulation Results and Discussion

we present simulation results for OTFS using various detection methods introduced in this paper. We evaluate the performance of different OTFS frame structures using different data detection techniques that have been explained in the previous section in terms of error performance. The simulation parameters have been shown in Table I. Figure 10 to Figure 13 show the bit error rate (BER) performance of the OTFS schemes with $M = N = 64$ using OPSK Modulation techniques under standard EPA and EVA channel model with a receiver speed of 350 km/h. The four-frame structure chosen as ZP-OTFS, CP-OTFS, RZP-OTFS, and RCP-OTFS which have been shown in Figure 10 to Figure 13, respectively.

Table 1: Simulation Parameters

Simulation Parameters	Value
Modulation Order	QPSK, 16 and 64 QAM
Number of Symbols (N)	16
Number of Subcarriers (M)	64
Subcarrier Spacing (Δf)	15 kHz
Number of OTFS frames	300
Carrier Frequency (fc)	4 GHz
Channels model	EPA, and EVA
Speed	350 /h

These figures compare four receiver detection which has been considered in this paper: a single-tap frequency domain equalization, LMMSE detection, an MPA detection (15 iterations), and an MRC detection (15 iterations). We can observe that the MRC detection offers the best performance followed by LMMSE and MPA, respectively. The lowest complexity single-tap equalizer offers the worst performance. In the EVA channel model, It can be seen that the MRC algorithm achieves about 4 dB gain over the single-tap equalizer algorithm at a BER of 10^{-3}.

For the best error performance, the delay and Doppler resolution need to be sufficient to resolve all the significant channel paths into distinct delay and Doppler bins, which is convenient for large frames. For several subcarriers $M = 64$, the delay resolution $1/M\Delta$f is equal to approximately 1000 ns.

In the EVA channel model, it has 9 delay paths and a maximum delay spread of 2510 ns which can be separated into multiple delay bins at M = 64 and coherently combined at the receiver. On the other hand, the EPA channel model has 7 paths with a maximum delay spread of 410 ns. none of the multipath is separable along the delay domain, since all the paths fall within one delay bin of size 1000 ns.

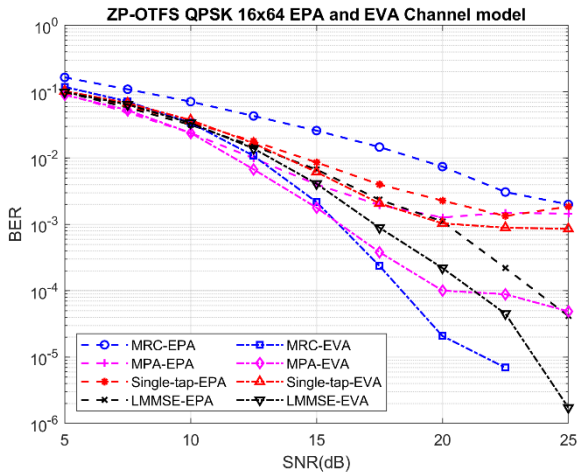

Figure 9: The BER performance of ZP-OTFS using a single-tap equalizer, LMMSE, MPA, and MRC with QPSK modulation under the EPA and EVA Channel model.

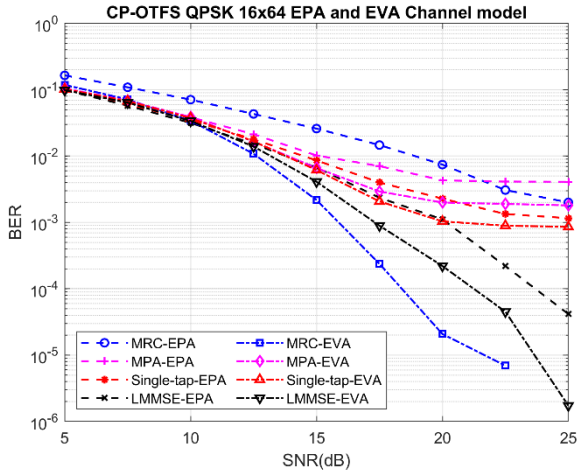

Figure 10: The BER performance of CP-OTFS using a single-tap equalizer, LMMSE, MPA, and MRC with QPSK modulation under the EPA and EVA Channel model.

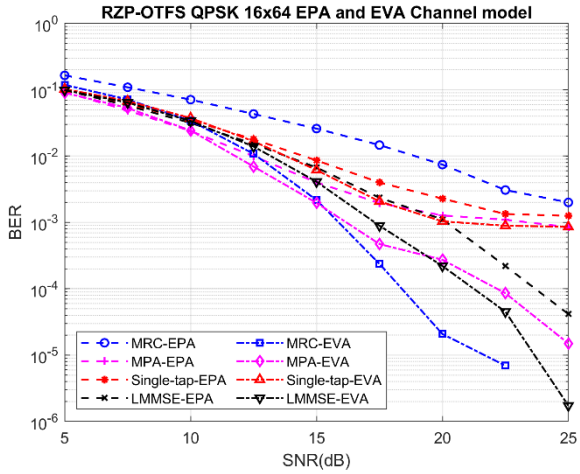

Figure 11: The BER performance of RZP-OTFS using a single-tap equalizer, LMMSE, MPA, and MRC with QPSK modulation under the EPA and EVA Channel model.

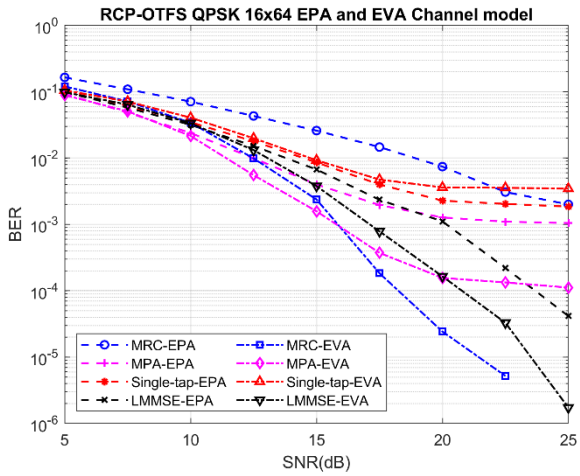

Figure 12: The BER performance of RCP-OTFS using a single-tap equalizer, LMMSE, MPA, and MRC with QPSK modulation under the EPA and EVA Channel model.

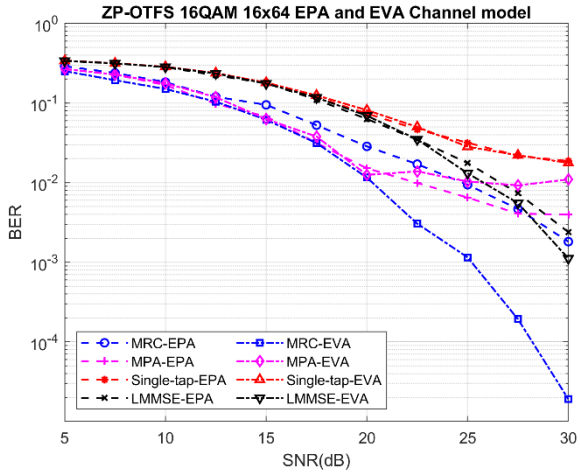

Figure 13: The BER performance of CP-OTFS using a single-tap equalizer, LMMSE, MPA, and MRC with 16QAM modulation under the EPA and EVA Channel model.

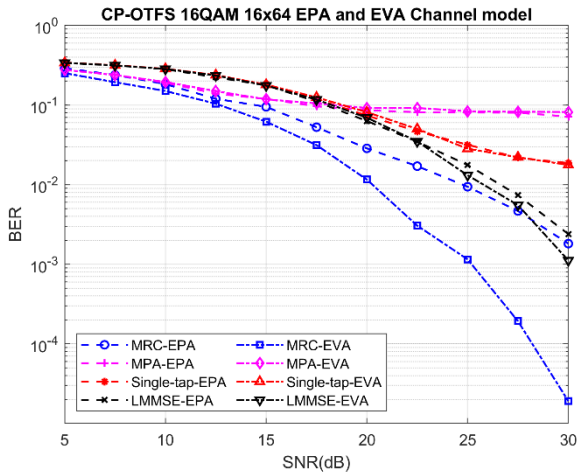

Figure 14: The BER performance of CP-OTFS using a single-tap equalizer, LMMSE, MPA, and MRC with 16QAM modulation under the EPA and EVA Channel model.

This is illustrated in Figure 10 to 13, where OTFS performs the worst for the EPA channel model. For small sizes of M, the paths falling into the same delay bin can still be separated along the Doppler domain by increasing N, thereby taking advantage of the channel Doppler diversity. Figure 14 to Figure 17 show the bit error rate (BER) performance of the OTFS schemes with $M = N = 64$ using 16-QAM Modulation techniques under standard EPA and EVA channel model with a receiver speed of 350 km/h. The four-frame structure chosen as ZP-OTFS, CP-OTFS, RZP-OTFS, and RCP-OTFS which have been shown in Figure 10 to Figure 13, respectively. these figures compare four receiver detection which has been considered in this paper: a single-tap frequency domain equalization, LMMSE detection, an MPA detection (15 iterations), and an MRC detection (15 iterations). As the same as the QPSK modulation in Figure 10 to 13, We can observe that the MRC detection offers the best performance followed by LMMSE and MPA, respectively. The lowest complexity single-tap equalizer offers the worst performance. Additionally, the OTFS in EVA is outperform the EPA channel.

Figure 18 show the error performance of the MPA algorithm for different OTFS frame structure under the EPA and EVA Channel model. It can observe that the four different frame structures have achieved approximately the same BER performance. The main difference between the four schemes is in throughput and complexity. In Figure 19, The BER performance of CP-OTFS using a single-tap equalizer, LMMSE, MPA, and MRC detection algorithms with different modulation orders (QPSK, 16 QAM, and 64QAM) under the EVA Channel model has been shown.

6. CONCLUSION

In this paper, we studied the performance analysis of OTFS systems over high-mobility channels. We first explained the variants of OTFS frame structure, where the waveform is transmitted with a CP or ZP added to each OTFS frame or block. Then, we described four data detection algorithms for OTFS and demonstrated the main difference between these different detection algorithms Furthermore, the simulation results have been performed under different channel models. The results show that the MRC algorithm outperforms the other detection methods. Our future work will focus on channel code design for OTFS systems to improve error performance.

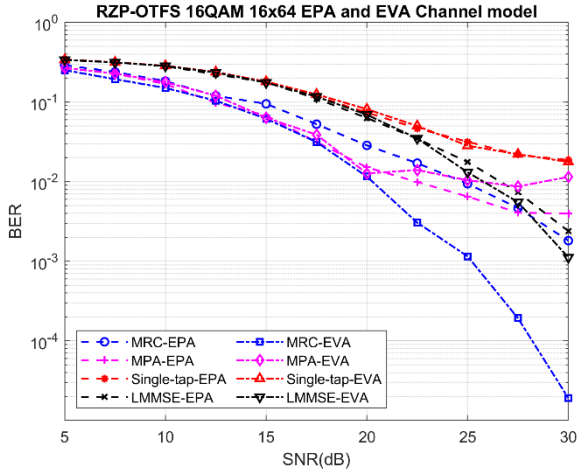

Figure 15: The BER performance of RZP-OTFS using a single-tap equalizer, LMMSE, MPA, and MRC with 16QAM modulation under the EPA and EVA Channel model.

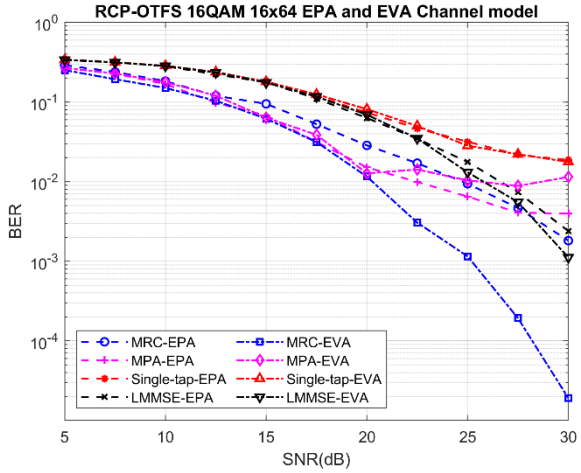

Figure 16: The BER performance of RCP-OTFS using a single-tap equalizer, LMMSE, MPA, and MRC with 16QAM modulation under the EPA and EVA Channel model.

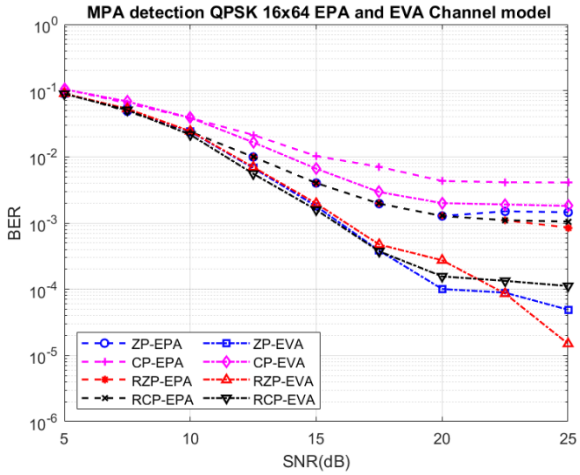

Figure 17: The BER performance of MPA detecion for differenct OTFS frame structure under EPA and EVA Channel model.

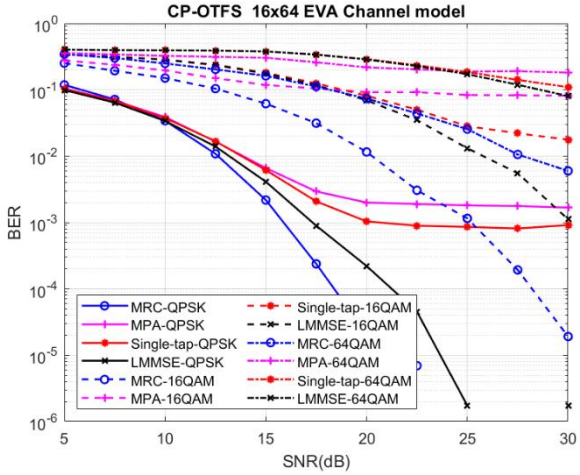

Figure 18: The BER performance of CP-OTFS using a single-tap equalizer, LMMSE, MPA, and MRC with different modulation orders (QPSK, 16QAM, and 64QAM) under the EVA Channel model.

2.1. Tested compound and doses

Hydroxyapatite nanoparticles (HAPNPs) were obtained from Riedel-de-Haën, Germany. Chitosan nanoparticles were purchased from Cognis Co., and curcumin nanoparticles were purchased from Nanotech Egypt. The doses of nanoparticles of hydroxyapatite (HAP NPs), chitosan (CSNPs) and curcumin (CurNPS) were 300 mg/kg BW, 280 mg/kg BW and 15 mg/kg BW according to Abdel-Gawad and Awwad (2010), Tang et al. (2007) and Yadav et al. (2012).

2.2 Animals and Experimental Design

Forty Albino male rats weighing 170-178g (11 weeks old) were used in the present study. Design of the experiment was approved by the local committee, and the protocol conforms to the guidelines of the National Institutes of Health. The animals were housed in clear plastic cages with hardwood bedding. Animals were maintained in a controlled atmosphere, a temperature of 25 ± 5 °C and 50-70% humidity with a 12 h light/day cycle.

2.3. Collection of blood and testes preparation

Animals were sacrificed by the end of the experimental period using isoflurane 100% (2 mg/Kg BW or equal 2% inhaled in dictator). Blood samples were collected by cardiac puncture and centrifuged for the separation of plasma (860 xg for 20 minutes) that was kept at -80 ˚C until analysis. Testes were immediately removed, washed using chilled saline solution (0.9%), and removed the adhering fat and connective tissues

3. Results

Data represented in Table 1 showed that treatment with hydroxyapatite nanoparticles (HAP NPs) alone caused significant (P<0.05) decrease in sperm count, sperm motility and significant (P<0.05) increase in abnormal sperm. Treatment with nanoparticles of chitosan (CSNPs) and curcumin (CurNPs) alone did not show any changes in semen characteristics. Treatment with the combination with CSNPs and CurNPs caused significant increase in motility, count and caused significant (P<0.05) decrease in abnormal sperms. The presence of CSNPs and CurNPs alone or in combination with HAP NPs mitigated its effects.

Table 1

Semen characteristics of male rats treated with nanoparticles of chitosan (CSNPs), curcumin (CurNPs) and hydroxyapatite (HAPNPs) and their combination

Experimental groups	Parameter		
	Sperm count (10^6/gm epididymis)	Sperm motility (%)	Abnormal sperm (%)
Control	55.3 ± 2.02^{b}	70.5 ± 3.80^{ab}	13.3 ± 0.85^{ef}
CSNPs	55.0 ± 2.74^{b}	69.8 ± 2.75^{ab}	14.0 ± 0.91^{e}
CurNPs	58.0 ± 1.78^{ab}	69.3 ± 2.66^{b}	13.7 ± 0.85^{e}
CS+CurNPs	64.3 ± 3.90^{a}	76.3 ± 2.43^{a}	11.0 ± 0.74^{f}
HAPNPs	24.0 ± 1.29^{e}	33.5 ± 1.71^{e}	29.5 ± 1.04^{a}
HAP+CSNPs	30.0 ± 1.08^{de}	40.0 ± 1.29^{de}	26.3 ± 0.85^{b}
HAP+CurNPs	35.0 ± 1.47^{cd}	43.8 ± 1.23^{cd}	23.8 ± 0.85^{c}
HAP+CS+CurNPs	40.3 ± 1.70^{c}	49.5 ± 1.44^{c}	18.5 ± 0.65^{d}

Data presented as Mean±SE. For each parameter, the groups with different superscript letters are significantly differ, p<0.05.

Testosterone, (17β-hydroxysteroid dehydrogenase (17β-HSD) and 17-ketosteroid reductase (17-KSR) were significantly (P<0.05) decreased, while LH and FSH levels were significantly (P<0.05) increased in rats treated with hydroxyapatite nanoparticles alone compared any other treated group. While, the combination of CSNPs and CurNPs or/ with HAPNPs showed a significant increase (P<0.05) in the testosterone, 17β-HSD and 17-KSR, and significant (P<0.05) decrease in FSH and LH hormone compared to the HAP NPs treated group (Table 2).

Table 2

Testosterone, follicle stimulating hormone (FSH), luteinizing hormone (LH), and testicular 17β-hydroxysteroid dehydrogenase and 17-ketosteroid reductase of male rats treated with nanoparticles of chitosan (CSNPs), curcumin (CurNPs) and hydroxyapatite (HAPNPs) and their combination

Experimental groups	Parameter				
	Testosterone (ngm/ml)	FSH (ngm/ml)	LH (ngm/ml)	17β-HSD (U/min/mg)	17-KSR (U/min/mg)
Control	5.2 ± 0.14^{b}	0.83 ± 0.05^{d}	0.58 ± 0.03^{d}	0.67 ± 0.038^{abc}	2.7 ± 0.24^{b}
CSNPs	5.1 ± 0.06^{b}	0.82 ± 0.03^{d}	0.58 ± 0.04^{d}	0.70 ± 0.039^{ab}	2.8 ± 0.27^{b}
CurNPs	5.4 ± 0.17^{ab}	0.79 ± 0.05^{d}	0.56 ± 0.04^{d}	0.67 ± 0.055^{ab}	3.0 ± 0.25^{ab}
CS+CurNPs	5.8 ± 0.13^{a}	0.76 ± 0.04^{d}	0.50 ± 0.02^{d}	0.78 ± 0.076^{a}	3.6 ± 0.38^{a}
HAPNPs	2.7 ± 0.08^{e}	1.35 ± 0.07^{a}	1.01 ± 0.05^{a}	0.52 ± 0.032^{c}	1.5 ± 0.11^{c}
HAP+CSNPs	3.4 ± 0.12^{d}	1.26 ± 0.03^{ab}	0.90 ± 0.04^{ab}	0.55 ± 0.042^{bc}	1.8 ± 0.10^{c}
HAP+CurNPs	3.7 ± 0.26^{d}	1.20 ± 0.05^{b}	0.86 ± 0.05^{bc}	0.56 ± 0.037^{bc}	1.5 ± 0.11^{c}
HAP+CS+CurNPs	4.5 ± 0.19^{c}	1.04 ± 0.03^{c}	0.77 ± 0.02^{c}	0.62 ± 0.027^{bc}	2.1 ± 0.09^{c}

Data presented as Mean±SE. For each parameter, the groups with different superscript letters are significantly differ, $p<0.05$.

Expression of uncoupling protein 2 (UCP2) and mitochondrial transcription factor A (mTFA) in testes are presented in Figure (1). The rats supplemented with chitosan alone or in combination with curcumin have non-significant higher expression level of UCP2, while the rats treated with curcumin alone have non-significant decline in the expression of UCP2. On the other hand, rats exposed to hydroxyapatite resulted in significant induction in the testicular expression of UCP2. The co-treatment of CSNPs and CurNPs to HAPNPs in the combination group showed significant decline in the induction of expression of UCP2 and completely normalized its values to the control (Figure 1). CSNPs supplementation alone or in combination with curcumin has significantly induced mTFA expression compared to control rats. HAPNPs significantly suppressed the expression of mTFA. CSNPs and CurNPs alone or in combination with HAP NPs normalized the expression of mTFA (Figure 1).

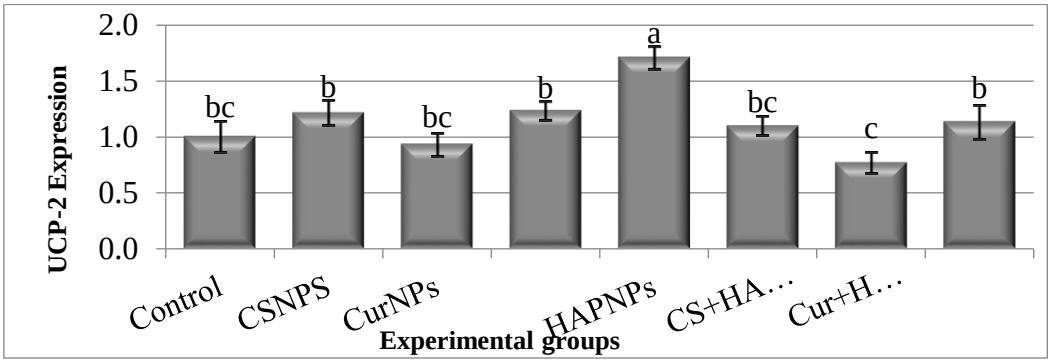

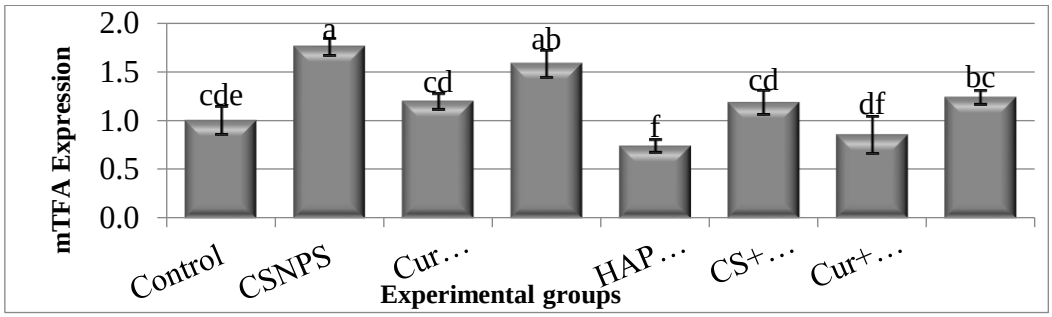

Figure 1: Testicular expression of uncoupling protein 2 (UCP2) and mitochondrial transcription factor-A (mtTFA) of male rats treated with chitosan (CSNPs), curcumin (Cur-NPs), hydroxyapatite (HAP NPs) nanoparticles and their combination.
Not sharing common superscript letters (a, b, c d, e and f) were significantly different, $p<0.05$.

Testes thiobarbituric acid-reactive substances (TBARS) and nitric oxide (NO) were significantly increased in rats treated with HAPNPs alone (Figure 2). Treatment with CSNPs and CsNPs alone or in combination with HAPNPs showed a significant decrease in the levels of NO and TBARS. GPx, GST, CAT, SOD, GSH and TAC activities were significantly ($P < 0.05$) decreased in rats exposed to HAPNPs (Figure 3). While, the presence of either chitosan or curcumin alone or in combination with HAPNPs was capable to increase the activities of GPx, GST, CAT, SOD, TAC and GSH and decrease TBARS and NO levels compared to HAPNPs treated group (Figs. 2 and 3). Chitosan or curcumin nanoparticles alone or in combination have showed no significant effect on the level of 8-OHdG compared to the control group. HAPNPs supplementation resulted in significant elevation in the level of testicular 8-OHdG by about 3-fold compared to the control group. While, the co-supplementation with CSNPs alone or in combination with CurNPs has significantly corrected and completely normalized the level 2-OHdG in rats supplemented with HAPNPs (Figure 2).

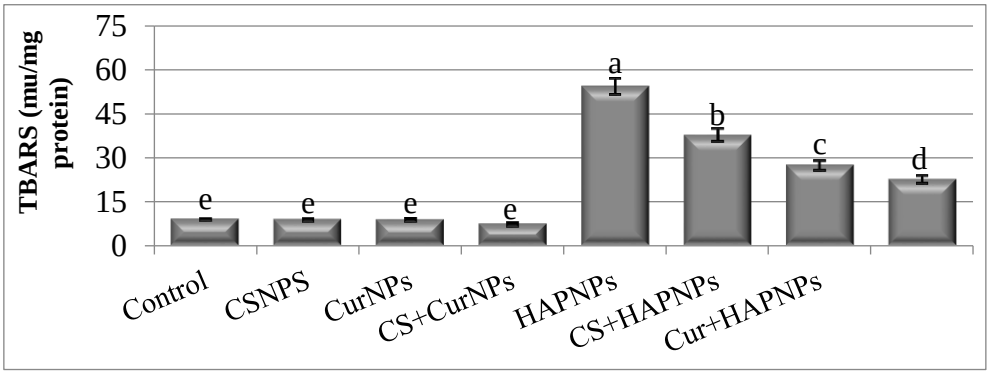

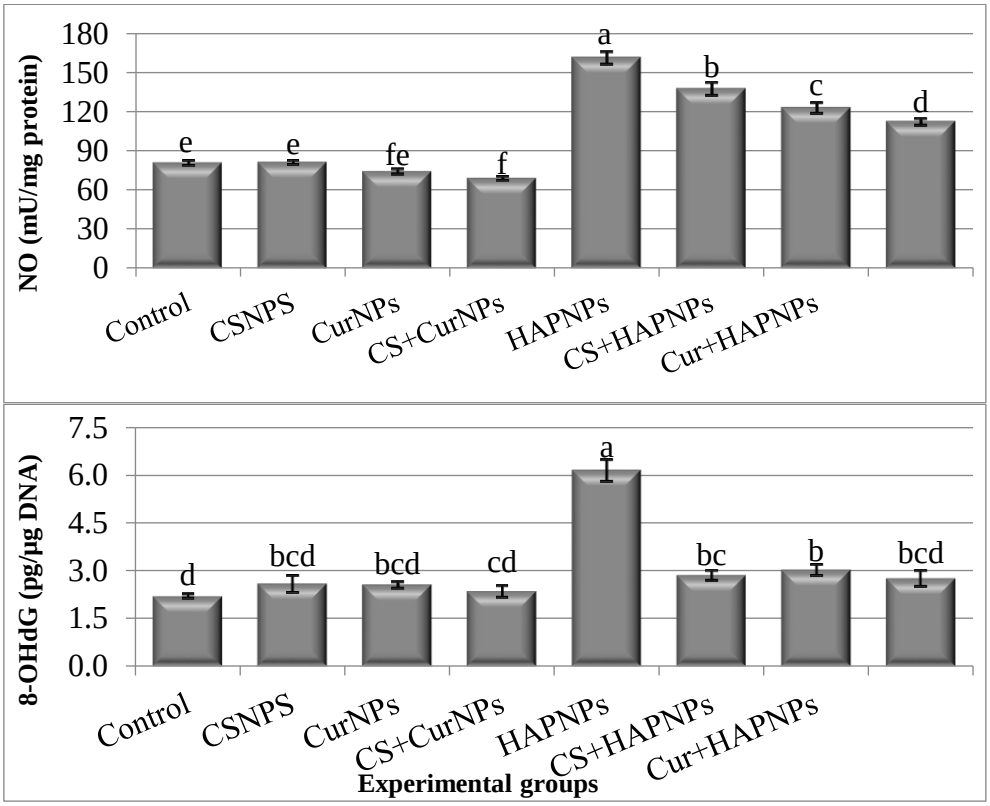

Figure 2: Testes thiobarbituric acid-reactive substances (TBARS), nitric oxide (NO) and 8-OH-2-deoxygunaine (8-OHdG) of male rats treated with nanoparticles of chitosan (CSNPs), curcumin (CurNPs) and hydroxyapatite (HAPNPs) and their combination.

Not sharing common superscript letters (a, b, c d, e and f) were significantly different, $p<0.05$.

4. Discussion

Testicular tissues and sperms are extremely sensitive to oxidative damage because of its high membrane concentration of polyunsaturated fatty acids, active generation of free radicals and a low level of defensive enzymes. Our results showed elevation in TBARS which is the index of lipid peroxidation due to HAPNPs exposure. The peroxidation of lipid membrane of sperm affects the fertility because sperms are dependent upon the integrity and fluidity of their cell membrane for proper function. Without proper membrane fluidity, enzymes are activated, which can lead to impaired motility, abnormal structure, loss of viability, and ultimately death to the sperm or teratozoospermia (Sikka et al., 1995). Lipid peroxidation may be cause damage to basement membrane of seminiferous tubules, Sertoli cells and Leydig cells which lead to imbalance in the production of testosterone FSH and LH hormones. Cell damages including loss of cell lines, such as round and elongated spermatids as well as spermatogonia cells, are the consequence of this imbalance; because, one of major regulators for FSH and LH hormones is the negative feedback exerted by testosterone hormone which is produced by Leydig cells (Rodwell et al., 2015). Our results showed increase in testes nitric oxide (NO) of rats treated with HAPNPs and could be there is a correlation between excess NO and the decline in second messenger cAMP. Guo et al. (2005) suggested that cAMP play essential role for the mediation for the action of gonadotropin in the synthesis of pregenolone in Leydig cells from cholesterol. The results obtained by Guo et al. (2005) suggested that decrease in cAMP caused decline in the production of testosterone.

At the molecular level, our results revealed that HAPNPs-induced oxidative stress in testicular tissues that caused significant elevation in the oxidative DNA marker; 8-hydroxy-deoxyguanin (8-OHdG). Mangerich et al. (2012) reported that ROS are highly reactive with DNA. 8-oxo-G is one of the prominent forms of oxidativelly generated DNA base modifications and considered to be a sensitive marker of oxidative DNA damage (Cooke et al., 2003). If the repair mechanism didn't remove 8-OH-dG formed in DNA may cause guanine (G) to thymine (T) substitution upon replication, alternatively, 8-OH-dG (in the nucleotide pool) may be mis-incorporated opposite adenine (A) producing A-C substitution (Cheng et al., 1992). These mutagenic potentials of 8-OH-dG formation may indicate the hazards of HANPs-induced genotoxicity.

Conclusion

Finally, from the above discussion it was clear that, the exposure to HAPNPs have toxicity on male reproductive system at different levels including, histological structure, inmmunohistochemical reactivity toward PCNA, sperm count and quality, steroidogenesis, oxidative stress, DNA damage, cytokine production, and gene expression of mTFA and UCP2. Our data delivers suggestions for using CSNPs and CurNPs alone or in combination to mitigate the reproductive deteriorations induced by HAPNPs.

Disclosure

This research did not receive any specific grant from funding agencies in the public, commercial or not-for-profit sectors. There is no Conflict of Interest

References

Asyaz S, Hussain I, Khan FU, Khan MA, Khan IU. Evaluation of chemical analysis profile of Citrullus colocynthis growing in southern areas of Khyber Pukhtunkhwa Pakistan. World appl. Sci. J. 2010; 10(4): 402-405.

Boreiko CJ, Rossman TG. Antimony and its compounds: Health impacts related to pulmonary toxicity, cancer and genotoxicity. Toxicol. Appl. Pharmacol. 2020; 403: 115156.

Chen Y, Sa Y, Wang G, Pan X, Zhen Y, Cheng X, Liu B. The protective effects of Citrullus colocynthis on inhibiting oxidative damage and autophagy-associated cell death in Parkinson's disease. J. Taiwan Inst. Chem. Eng. 2019; 100: 18-25.

Halpern SD, Ubel PA, Caplan AL. Solid-organ transplantation in HIV- infected patients. N Eng1J Med. 2002; 347: 284-7.

Teodoro JS, Rolo AP, Palmeira CM. The NAD ratio redox paradox: why does too much reductive power cause oxidative stress? Toxicol. Mech. Methods 2013; 23(5): 297–302.

Yang L, Wang CZ, Ye JZ, Li HT. Hepatoprotective effects of polyprenols from Ginkgo biloba L. leaves on CCl4-induced hepatotoxicity in rats. Fitoterapia 2011; 82(6): 834-840.

For articles with more than six authors: List the first six authors followed by et al.

Rose ME, Huerbin MB, Melick, Marion SW, Plamer AM, Schiding JK, et al. Regulation of interstitial excitatory amino acid concentrations after cortical contusion injury. Brain Res 2002; 935:40-6.

Systematic Reviews and Meta-analysis:

Manuscripts should follow the Cochrane Collaboration methodology for publication.